International Journal of Physics and Applications

E-ISSN: 2664-7583
P-ISSN: 2664-7575
IJOS 2024; 6(1): 110-121

www.physicsjournal.in
Received: 06-02-2024
Accepted: 11-03-2024

SA Mahdi
Department of Physics, College of Science, Tikrit University, Tikrit, Iraq

M Ellouze
University of Sfax, Faculty of Sciences of Sfax, LMEEM, B. P. 1171, 3000, Sfax, Tunisia

Abdul Samee Fawzi
Department of Physics, College of Science, Tikrit University, Tikrit, Iraq

Corresponding Author:
SA Mahdi
Department of Physics, College of Science, Tikrit University, Tikrit, Iraq

Synthesis and analysis of [y($Mg_{0.5}Cd_{0.5}Fe_2O_4$) +[(1-y) [$Pb(_{1/3}BaLi_{2/3})$ O_3+$PbTiO_3$]] composites prepared via co-precipitation

SA Mahdi, M Ellouze and Abdul Samee Fawzi

DOI: https://doi.org/10.33545/26647575.2024.v6.i1b.87

Abstract
In this study, multiphase nanocomposites were synthesized through a three-phase pathway. The ferrite phase, ($Mg_{0.5}Cd_{0.5}Fe_2O_4$) [MCFO], enhances the material's magnetic and structural properties. The ferroelectric phase, [$Pb(_{1/3}BaLi_{2/3})$ O_3+$PbTiO_3$] [PBLTO], exhibits dielectric loss, stores electrical energy, and polarizes. Dual-phase compounds: [0.25($Mg_{0.5}Cd_{0.5}Fe_2O_4$) + 0.75 [$Pb(_{1/3}BaLi_{2/3})O_3$+$PbTiO_3$]] [A1] and [0.45($Mg_{0.5}Cd_{0.5}Fe_2O_4$) + 0.55 [$Pb(_{1/3}BaLi_{2/3})O_3$+$PbTiO_3$]] [A2],
were created by varying weight ratios of ferrite concentration. These compounds bridge the gap between the ferrite and ferroelectric phases and approach offers several advantages over traditional methods, including enhanced control over the morphology and properties of the resulting. The synthesis employed the chemical co-precipitation method at an annealing temperature of 550°C for two hours, the structural properties such as lattice constants (a, c), physical density (ρ_a) and density by X-ray diffraction (ρ_x-ray). The findings evidenced an increase in the lattice constant attributed to differences in atomic radii of elements, impacting X-ray intensity. Rietveld refinement analysis indicates that the space group for ferrite compounds is Fd-3 m, while for ferroelectric compounds it is P4/mmm. Furthermore, the study revealed that real and imaginary dielectric constants, as well as dielectric losses, demonstrate enhanced performance with increasing frequency at lower frequencies, aligning with the characteristic behavior observed in ceramic materials.
The saturation magnetization value remains relatively constant in the MCFO, A1, and A2 models, despite the decrease in saturation magnetization values with higher ferroelectric phase content (BTO). This suggests that the magnetic field value for saturation magnetization is not significantly affected by the ferroelectric phase content.

Keywords: Materials composite, X-ray diffraction, nanoparticles, co-precipitation method, magnetic properties

1. Introduction
The significant advancements in materials science and engineering have paved the way for the creation of composite materials, which are a combination of two or more distinct materials or phases. These materials possess unique properties that often surpass those of their individual components [1, 2].
Furthermore, its unique combination of mechanical, physical, and chemical properties grants it exceptional versatility. Unlike traditional materials, its characteristics can be tailored or enhanced to meet specific application requirements [3].
Nanoscience, a multidisciplinary field encompassing physics, chemistry, and biology, stands out from the exploration of the unique properties of materials at the nanoscale, where dimensions are measured in billionths of a meter. These properties are obviously different from those of bulk materials. "Nanotechnology," the most widely used branch, deals with the creation, characterization, manufacturing, and use of structures and devices made possible by manipulating their dimension and form at the nanometric scale [4].
The co-precipitation method was selected for preparing the composites in this study due to its efficiency and minimal sintering requirements. This method offers a fast-processing time, making it a suitable choice for researchers studying the properties of these materials.
G. Sathishkumar *et al*. (2010) synthesized Co-Ni-Zn ferrite using a chemical co-precipitation method, revealing reduced lattice constant and increased electrical insulation constant with increasing nickel ion concentration [5]. T. Yadavalli and his team (2016) prepared cobalt zinc

ferrite nanoparticles by a co-precipitation method using low temperatures, revealing a decrease in saturation magnetization value and nanoparticle size at temperatures ranging from 50 to 6000 °C [6]. M. S. Hossain *et al*. (2017) synthesized $ZnFe_2O_4$ nanoparticles using two methods: chemical deposition and solid-state reaction. Both methods produced single-phase structures with 5 nm particles. However, chemical deposition produced superparamagnetic samples with higher magnetization than those from the solid-state reaction [7].

2. Experimental details

Chemical co-precipitation was used to synthesize ($Mg_{0.5}Cd_{0.5}Fe_2O_4$) [MCFO] and [$Pb(_{1/3}BaLi_{2/3})$ O_3+$PbTiO_3$] [PBLTO] compounds. Additionally, a dual-phase material with different weight percentages of ferrite concentrations (y = 0, 0.25, 0.45, and 1) was synthesized. It was composed of [$y(Mg_{0.5}Cd_{0.5}Fe_2O_4)$ + (1-y) [$Pb(_{1/3}BaLi_{2/3})$ O_3+$PbTiO_3$] [MCFO – PBLTO].

MCFO, PBLTO, A1and A2 were the labels assigned to these samples, respectively.

The precursor materials were thoroughly mixed using an agate mortar, grinding and milling for half an hour to obtain the desired homogenous powder. Subsequently, the powders were compacted into pellets with a diameter of approximately 10 mm. These pellets were then subjected to a sintering process at 500°C for a duration of 2 hours. To promote enhanced crystallization, Finally, the pellets were gradually cooled to room temperature in an air environment.

XRD was used to measure the phase and cell parameters of the synthesized materials. The analyses were verified using the Rietveld method on a Panalytical X'PERT Pro diffractometer over an angular range of 10–80° with a step size of 0.026°. XRD measurements were performed at room temperature.

For the purpose of conducting insulation measurements, both opposing surfaces of each sample are coated with a thin layer of silver paste to achieve good ohmic conductivity, Using an HIOKI 3532-50 LCR Hi Tester.

The magnetic properties, represented by the magnetic hysteresis curve and the saturation magnetization of all samples, were determined using VSM EZ technology (Model 10 vibrating sample magnetometer) within the magnetic field range of (−10 to +10 T) at room temperature.

3. Results and discussion

3.1 Structural properties

X-ray diffraction (XRD) was used to study samples MCFO, PBLTO, A1, and A2 as shown in Figure 1. The ferrite samples showed spinel phase as the primary phase, A face-centered cubic (Fcc) structure was identified the samples crystallizing in a cubic system with the space group Fd-3m consistent with ICDD card number 96-153-9599, and the most intense peak at the (311) Miller index. PBLTO's crystal structure was tetragonal have the space group P 4/mmm, consistent with ICDD-96-154-2249 data. The dual phase of the compounds showed slight variation in phase percentages and absence of any unknown phase indicates the purity of the phases used in the production of these compounds.

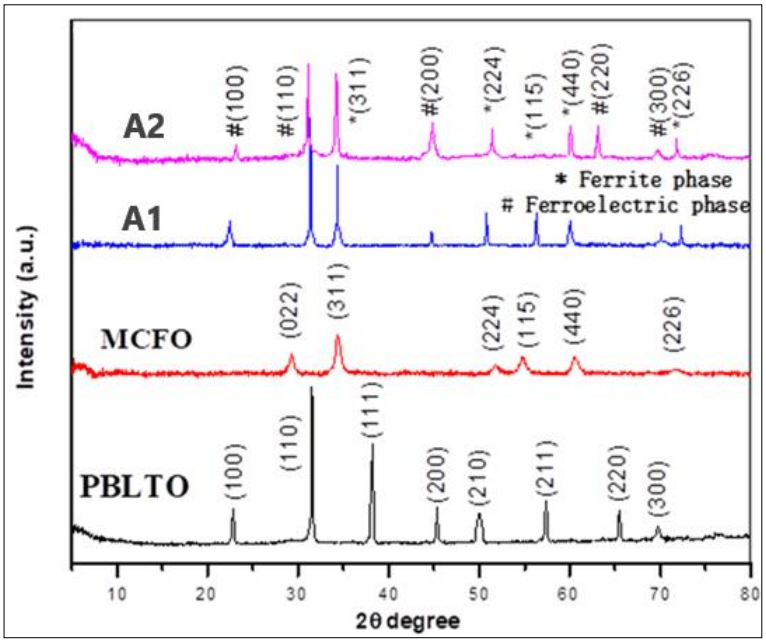

Fig 1: XRD patterns of MCFO, PBLTO, A1, A2 respectively

Additionally, the Miller coefficients matched those of the international card for the ferrite and ferroelectric phases mentioned earlier and displayed in Table (1) where the lattice constants of the compounds of ferrite, ferroelectric, and the dual phase of ferrite-ferroelectric were calculated according to the following mathematical relationships [8].

$$d_{hkl} = \frac{a}{\sqrt{h^2+k^2+l^2}}$$

$$\frac{1}{{d_{hkl}}^2} = \frac{h^2+k^2}{a^2} + \frac{l^2}{c^2}$$

Where (hkl) are Miller indices and (a, c) are lattice constants, and d is the value of the structural distance between parallel planes.

Table 1: Miller coefficients (hkl) and interlayer distance (d) obtained from X-ray diffraction for MCFO (*), PBLTO (#), A1, and A2, respectively

hkl	d_{std}(Å)	*MCFO*	*PBLTO*	*A1*	*A2*
		d (Å)	*d (Å)*	*d (Å)*	*d (Å)*
(100)#	*3.977*	-	*3.903*	*3.841*	*3.885*
*(220)**	*3.079*	*3.048*	-	-	-
(110)#	*2.834*	-	*2.837*	*2.819*	*2.838*
*(311)**	*2.626*	*2.611*	-	*2.583*	*2.597*
(111)#	*2.308*	-	*2.352*	-	-
(200)#	*1.989*	-	*1.999*	*2.019*	*2.019*
(210)#	*1.784*	-	*1.827*	-	-
*(224)**	*1.778*	*1.765*	-	*1.722*	*1.801*
*(115)**	*1.676*	*1.676*	-	*1.432-*	*1.633*
(211)#	*1.628*	-	*1.606*	-	-
*(440)**	*1.54*	*1.528*	-	*1.501*	*1.5*
(220)#	*1.406*	-	*1.424*	*1.251*	*1.301*
(300)#	*1.326*	-	*1.346*	*1.345*	*1.339*
*(226)**	*1.313*	*1.317*	-	*1.293*	

As for the lattice constant (a, c) of the compounds under study, it appears that an increase in the amount of the lattice constant for the double phase results from a change in the shift of the X-Ray spectrum and an increase in the concentration of the ferrite phase, which agrees with the results found in the literature [9, 10], also contribute to increase the crystalline size of both phases as well as increasing each density as a function of X-ray diffraction ($\rho_{x\text{-}ray}$) and physical density (ρ_a) (this results is agrees with W. Pabst and E. Gregorova [11]), and gradual decrease in porosity (P%), which depends on both types of density, can be calculated by applying following equations [12], Table 2.

$$\rho_{x_1} = \frac{8M}{N_A a^3}$$

$$\rho_{x_2} = \frac{M}{Na^2 c}$$

The same table also shows how the unit cell sizes of the compounds vary as the ferrite phase increases, with compound A having the largest unit cell size at 65.9 Å^3. The structural results are summarised in Table 2.

Table 2: Measurement of the Structural properties of MCFO, PBLTO, A1 and A2 respectively

Structural properties	*MCFO*	*PBLTO*	*MCFO – PBLTO A 1*	*MCFO – PBLTO A2*
a (Å)	*8.669*	*3.903*	*3.841*	*3.966*
c (Å)	*8.669*	*4.041*	*4.038*	*4.048*
c/a	*1*	*1.035*	*1.051*	*1.021*
Space group	*F d -3 m*	*P4/mmm*		
V(Å^3)	*651.489*	*61.558*	*59.574*	*63.672*
$\rho_{X\text{-}ray}$ (gm/cm^3)	*8.287*	*5.505*	*12.219*	*12.256*
ρ_a (gm/cm^3)	*7.233*	*3.629*	*8.685*	*8.965*
Porosity (%)	*12.725*	*34.072*	*28.92*	*26.852*

The Rietveld refinement method [13], implemented in the FullProf software [14], was used to analyze the diffractogram (Figure 2). This analysis confirmed that our MCFO sample crystallizes in a cubic structure with the space group Fd-3m at room temperature. The Rietveld method adjusts the calculated diffraction pattern to match the experimental data, allowing for precise determination of the crystal lattice parameters and atomic positions.

The difference pattern showed no unfitted peaks, suggesting that our sample MCFO had less than 1% of a second phase.

Figure 2, presents the experimental X-ray diffraction diffractogram refined measured (in red), calculated (in black), their differences (in blue) as well as the relative Bragg positions (in green) to the synthesized sample.

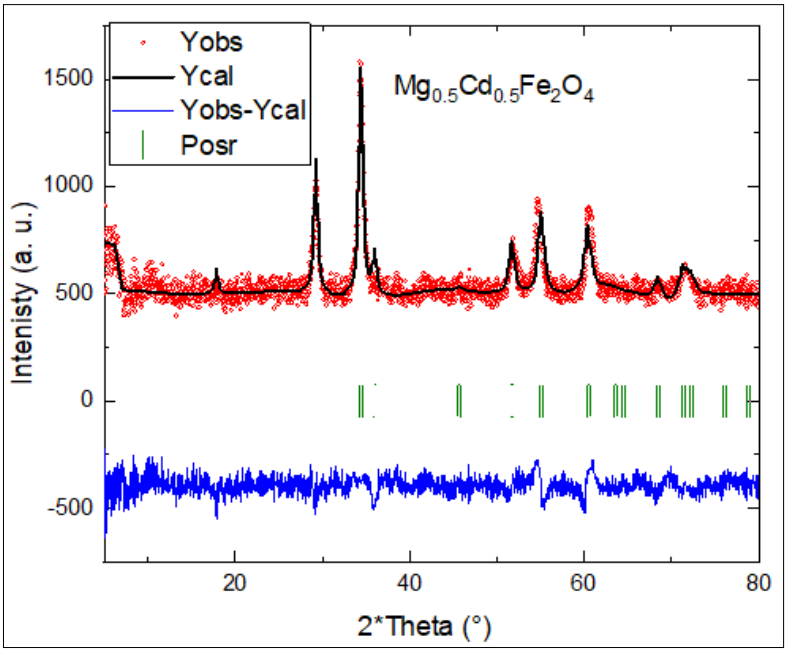

Fig 2: Measured and refinement powder X-ray diffraction pattern of MCFO sample

We were able to refine the mesh parameters for MCFO sample. An unconstrained refinement of the data yields the MCFO stoichiometries for the compound, with good values of χ2 parameter. The refinement results are summarised in Table 3.

Table 3: Refined structural parameters, Volume of a Unit Cell (V), <O-Mg-O> bond angle, d_{Fe-O} bond length, profile factor (Rp), weighted profile factor (R_{wp}), global chi-square (χ^2), for $Mg_{0.5}Cd_{0.5}Fe_2O_4$, n is the occupancy and the numbers in subscript represent the error bars

Atom Name	Position			
	x	y	z	n
Cd	0.000	0.000	0.000	0.185
Mg	0.000	0.000	0.000	0.315
Fe	0.625	0.625	0.625	1.00
O	0.375	0.375	0.375	1.00
v (Å^3)	a (Å)	b (Å)	c (Å)	
655.96	8.6888_2	8.6888_2	8.6888_2	
	R_p	R_{wp}	χ^2	
	4.26	4.22	3.64	
d_{Mg-O} (Å)	1.881			
d_{Fe-O} (Å)	2.172			
<O-Mg-O> (°)	144			
<O-Mg-O> (°)	90			
<O-Fe-O> (°)	135			
<O-Fe-O> (°)	45			

The $Mg_{0.5}Cd_{0.5}Fe_2O_4$ compound synthesized in this study differs from the $MgFe_2O_4$ compound described by L. Gazzetta *et al*. [15] in terms of magnesium content. While the current compound has a magnesium to iron ratio of 0.5:1, Gazzetta's compound has a 1:1 ratio. Additionally, the cell volume (521.66 Å³) and lattice constant (8.05 Å) of $MgFe_2O_4$ are smaller than those of the $Mg_{0.5}Cd_{0.5}Fe_2O_4$ compound (Table 2). This variation can be explained by the presence of cadmium., which has a larger ionic radius than magnesium. The substitution of magnesium with cadmium leads to an expansion of the lattice and an increase in cell volume.

The "Diamond" program was used to model the unit cell and calculate the distances between magnesium, cadmium, and iron ions, respectively, and the nearest oxygen ion using refined structural parameters for the MCFO sample, Figure 3. This approach allowed for a more accurate determination of the interatomic distances within the crystal structure as shown in table (3).

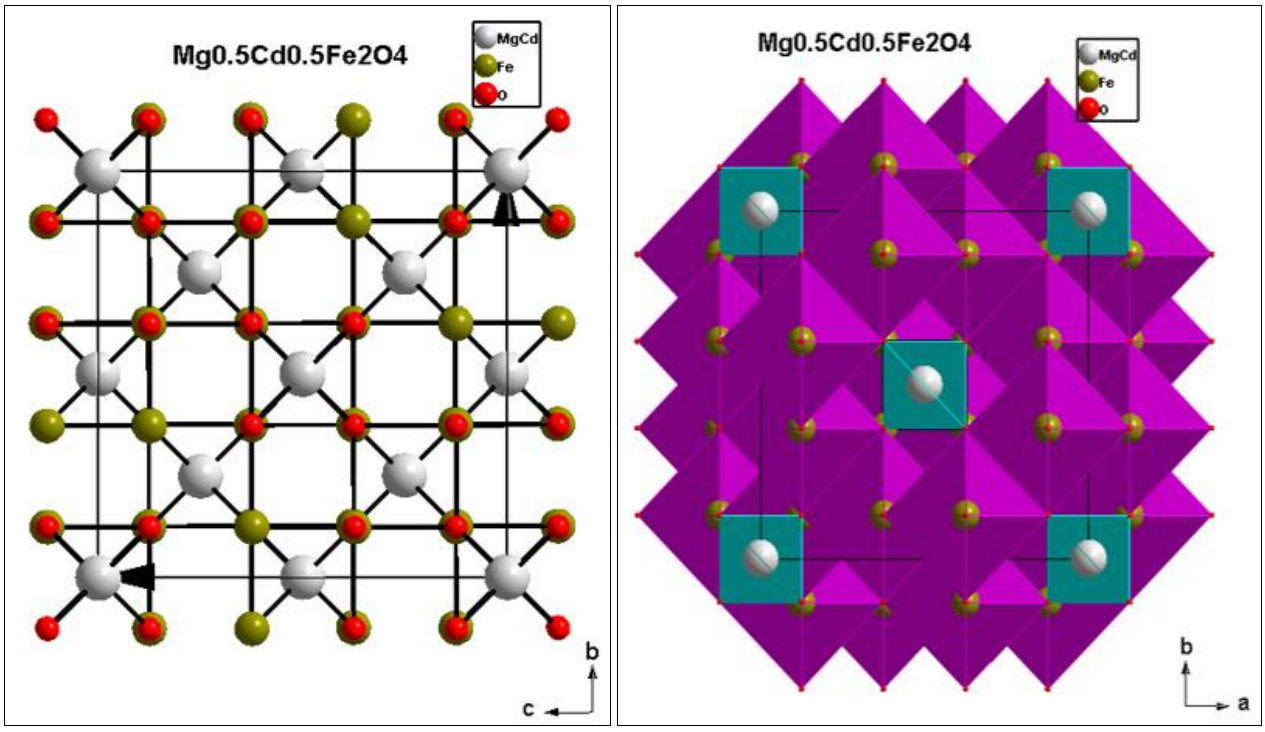

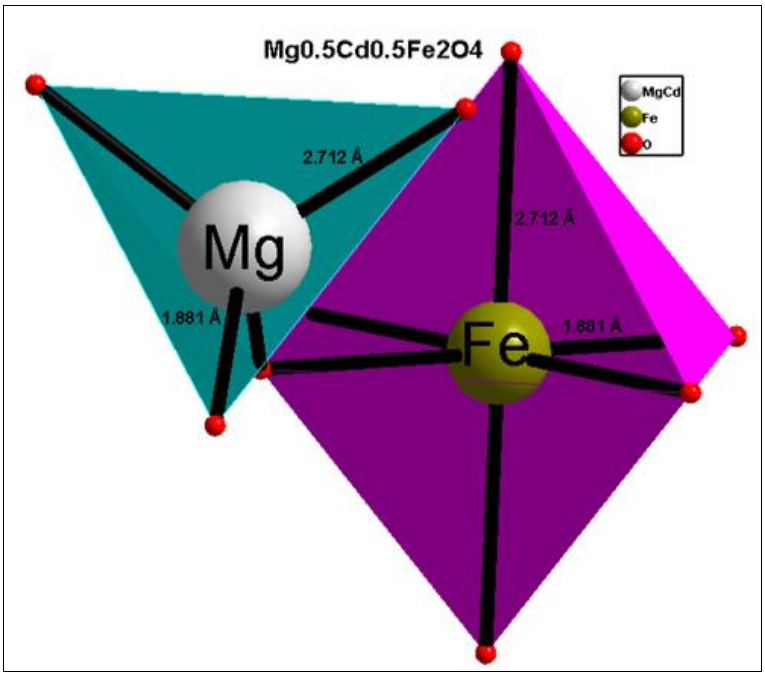

Fig 3: Crystal structure and Octahedra of $Mg_{0.5}Cd_{0.5}Fe_2O_4$ sample

The crystallite size (D_{SC}) was determined using the Scherrer equation, which relates the broadening of X-ray diffraction (XRD) peaks to the size of the crystallites [8].

$$D_{sc} = \frac{K\lambda}{\beta\cos\theta}$$

We also calculated the crystallite size (D_{WH}) using the Williamson-Hall method, which takes into account both the size and strain contributions to peak broadening. W-H equation given by [16].

$$\beta\cos\theta = K\lambda/D_{WH} + 4\varepsilon\sin\theta$$

where β is the full width at half maximum of the Bragg peaks, θ is the diffraction angle of the peaks, and λ is the wavelength of CuKα radiation (1.5406Å) and the strain-induced coefficient on crystallite size is ε =Δd⁄d. Using the intercept as the vertical axis, we can calculate the value of ε from the slope of the βcosθ vs. 4sinθ plot (Fig. 4., D_{WH} has been computed from (kλ/D_{WH}=intercept). Table (3) summarizes the calculated values for the D_{SC}, D_{WH} (crystal sizes) and D_P (D_P physical grain size measured by SEM).

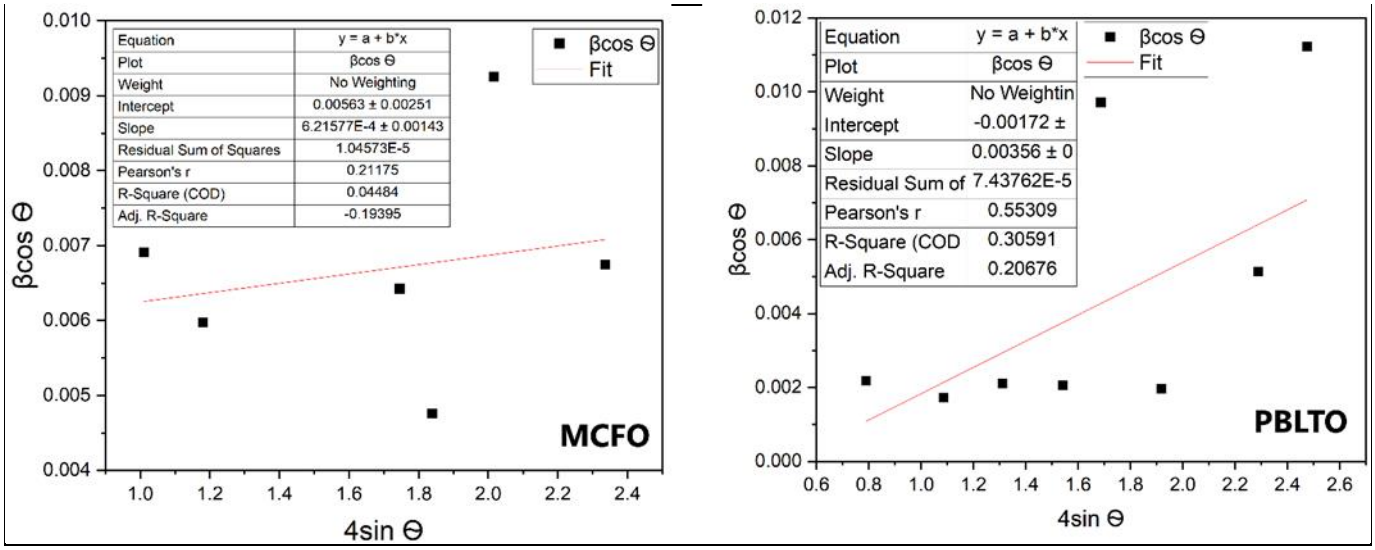

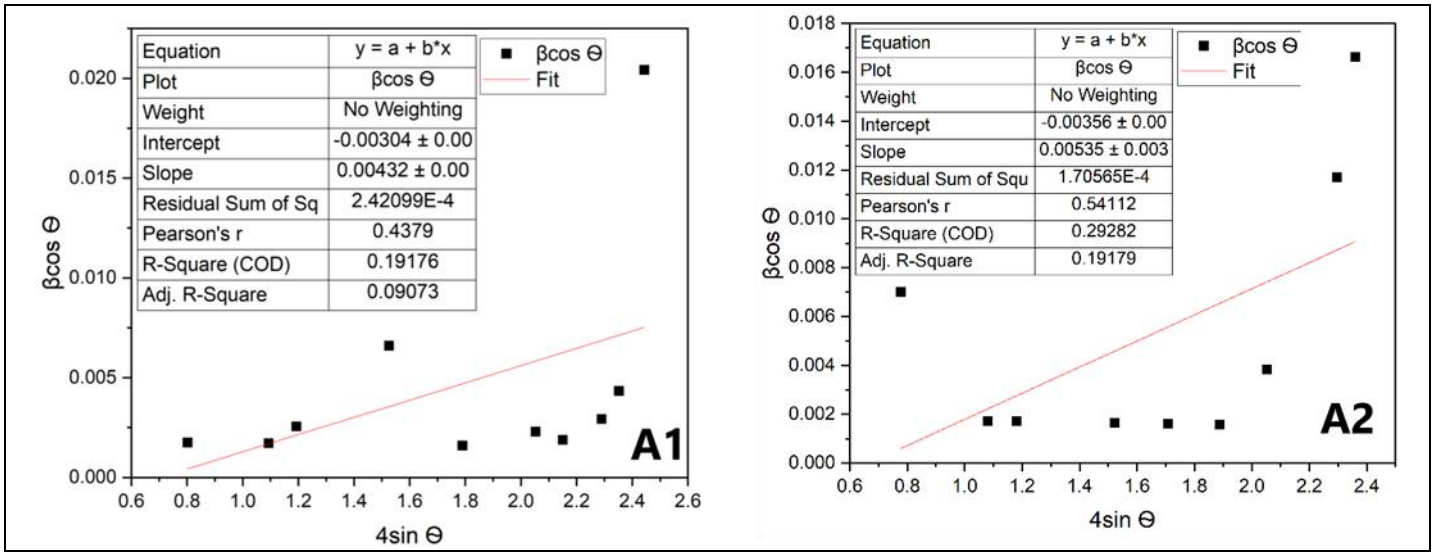

Fig 4: Williamson-Hall analysis plots of MCFO, PBLTO, A1 and A2 respectively

The results presented in Table 4, demonstrate that the crystallite size in each sample exhibits an approximate order of magnitude variation. Notably, this variation is only slight in relation to the physical grain size. This observation suggests that the grains within the powders possess a polycrystalline structure.

Table 4: Calculated values for the D_{SC}, D_{WH} (crystal sizes) and D_p(grain size) of MCFO, PBLTO, A1, A2 respectively

Crystallite size	MCFO	PBLTO	A 1	A2
D_{sh} (nm)	23.224	80.689	40.648	38.697
D_{W-H} (nm)	28.355	80.613	45.61	38.948
D_p (nm)	30.26	32.48	50.41	48.41

3.2 Analysis of scanning electron microscopy SEM

The SEM micrographs revealed significant morphological changes due to variations in the composition of the compounds MCFO, PBLTO, A1, and A2. As shown in Figure 5, the microstructure was homogeneous with spherical particles and a narrow particle size distribution. Agglomeration of particles led to a decrease in porosity and an increase in the size of the granular structure. The presence of agglomerated areas in the FE-SEM images is likely due to the natural interaction between magnetic nanoparticles and the thermal process, a tendency for agglomeration commonly observed in nanocrystalline spinel ferrites [17]. The ferroelectric samples exhibited a porous structure characterized by homogeneous spherical and polyhedral particles. This porous structure is attributed to the release of excess gases during the combustion method [18]. Furthermore, the results show an increase in grain size with increasing ferrite and cadmium concentrations. This can be attributed to the differences in the ionic radii of Cd^{+2} and Mg^{+2}, which affect grain size. This finding is consistent with the outcomes of the synthetic properties studied through XRD, indicating a pure crystal structure with a homogeneous microscopic structure. The average grain size (Dp) was calculated from the SEM images by considering the maximum number of particles shown in Figure 6. These results are summarized in Table 4.

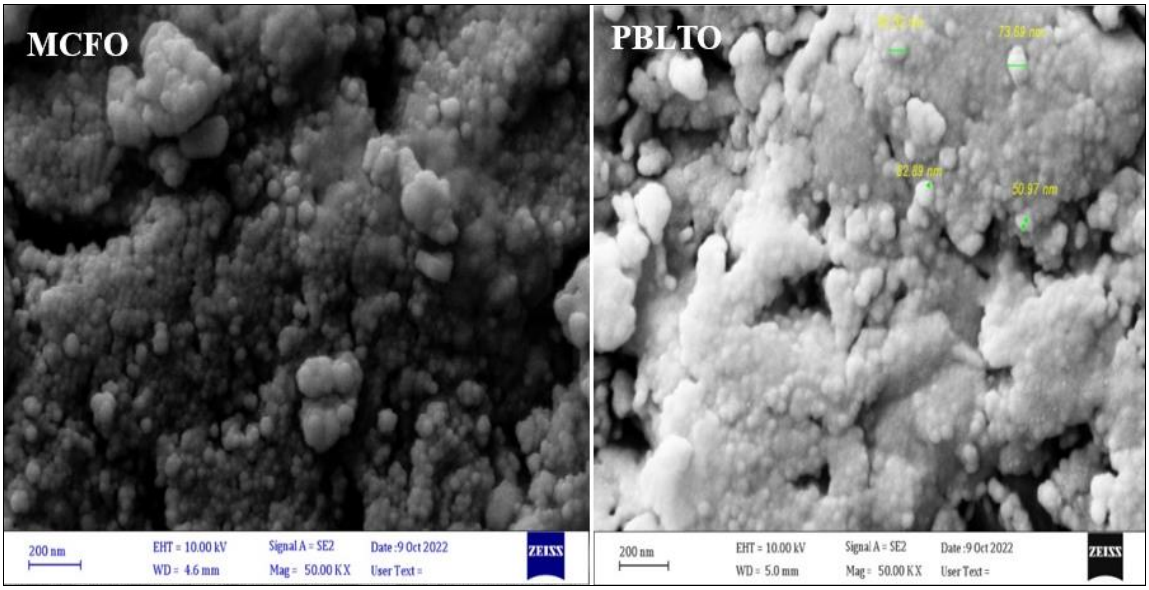

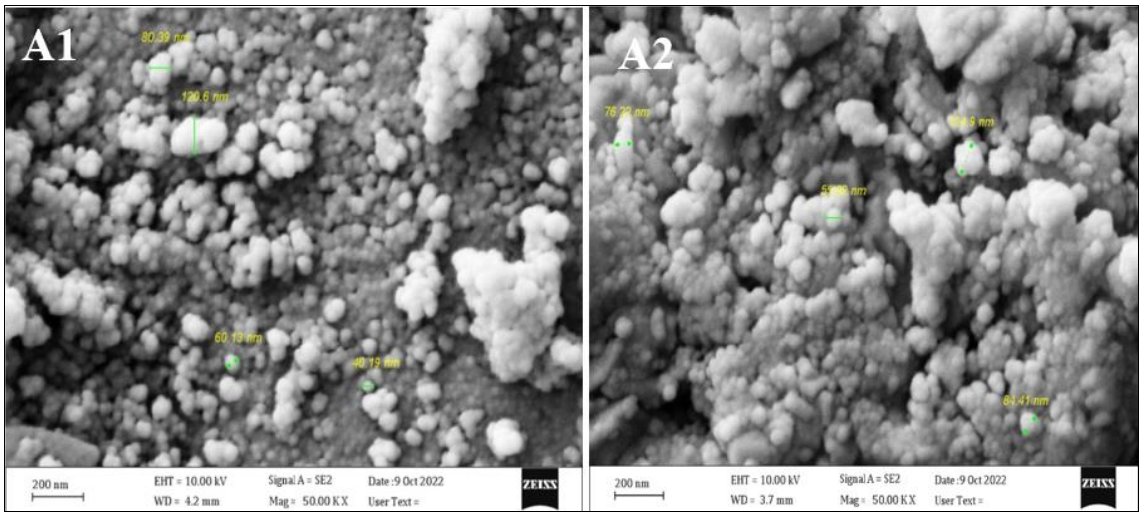

Fig 5: The SEM Images of MCFO, PBLTO, A1 and A2 respectively

The results were further corroborated by Energy-dispersive X-ray analysis (EDAX), a technique employed for nanoparticle measurement using SEM. EDAX revealed the elemental composition of the compounds MCFO, PBLTO, A1, and A2, as depicted in Figure 6. The figure showcases prominent peaks representing the weight percentages of elements in each model. Notably, lead (Pb) exhibits the highest weight percentage in the double-phase compounds.

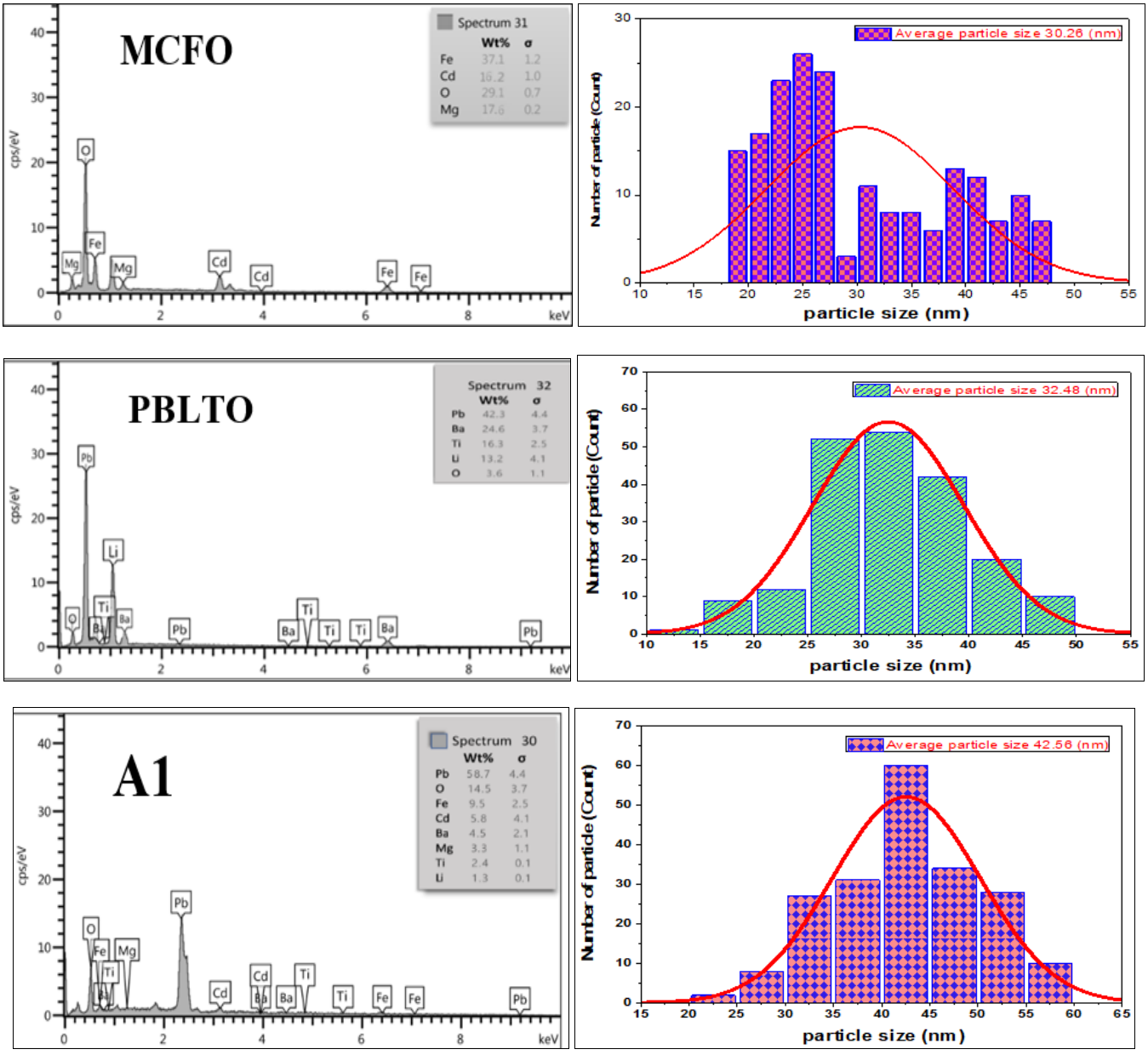

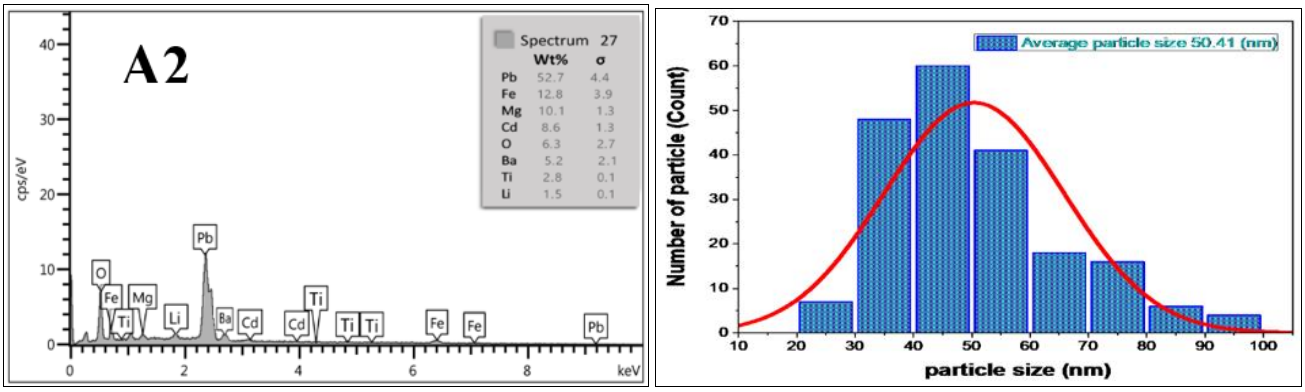

Fig 6: Average grain size distribution and EDAX plots of MCFO, PBLTO, A1, A2 respectively

3.3 Analysis of insulation properties

Figures 7 and 8 show the frequency dependence of the real (ε') and imaginary (ε") parts of the dielectric constant for models A2, A1, MCFO, and PBLTO at room temperature across the range (100H_Z -5MH_Z). according to the following mathematical relationships [19].

$$\varepsilon' = \frac{C\,d}{\varepsilon_0\,A}$$

$$\varepsilon'' = \varepsilon' \tan\delta$$

Where: (C): Capacitance (F), (d): Inter-plate distance of the capacitor (m), (ε_0): Permittivity of free space, a constant value of 8.85*10^{-12} (F/m), (A): Cross-sectional area of the insulator (m^2).

The dielectric constant values exhibit a peak at lower frequencies, followed by a rapid decline as frequency increases until it stabilizes. Notably, at frequencies of (4500 H_Z) for the real component and (3000 H_Z) for the imaginary component and below, a few polarizations of all types (polarized, electronic, ionic, dipole, and space) attains a high value.

This dielectric behavior is attributed to the polarization process of vacuum charge, which possesses a significantly larger mass compared to other types, as it represents a large group of charges that accumulate at crystal defects or voids, which leads to the generation of a local accumulation of charges that stimulates opposite charges on the other side, thus leading to the emergence of dipoles in the material, and when the frequency increases to more than (4500 H_Z) or (3000 H_Z) for the real and imaginary dielectric constant, respectively, we find a sharp decrease in the values of the dielectric constant, and this indicates that within this range of frequencies the period of polarization of the vacuum charge ends.

The dipoles responsible for the directional polarization are unable to keep up with the change in the direction of the applied electric field and direct itself towards it, and this would lead to a decrease in the values of the dielectric constant [20].

It is also noted that the highest value is for the PBLTO compound, then A1, A2, and MCFO. respectively, with a slight difference between the real and imaginary dielectric constant values.

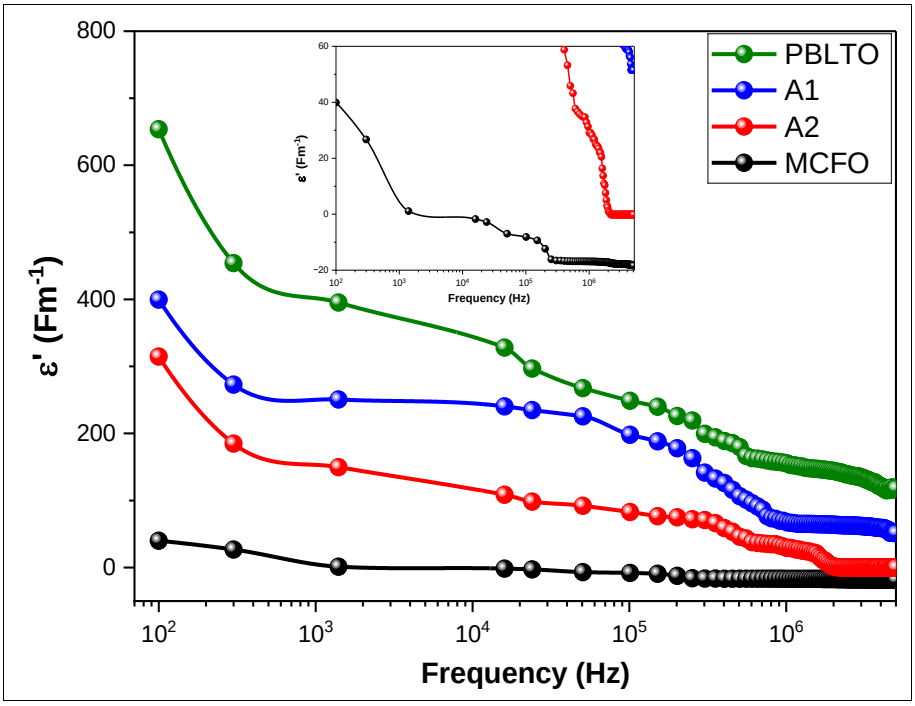

Fig 7: Variation of Real dielectric constant (ε') with frequency for MCFO, PBLTO, A1 and A2 respectively

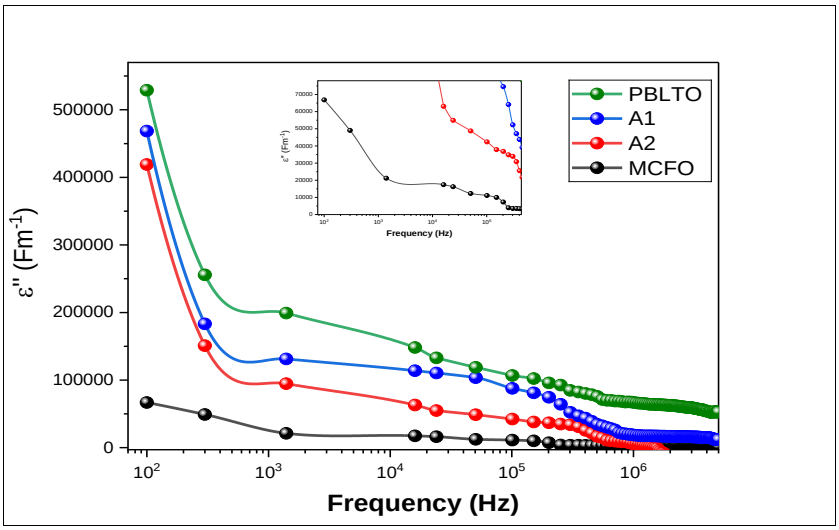

Fig 8: Variation of Imaginary dielectric constant (ε") with frequency for MCFO, PBLTO, A1 and A2 respectively

Figure (9) depicts the insulator loss or the tangent of the loss angle (tanδ) with frequency at room temperature for the models (MCFO, PBLTO, A1, A2). It is observed that the highest values of the tangent of the loss angle at lower frequencies stem from a significant relationship between insulation and the conduction mechanism behavior. In ferroelectrics, When the electric charge carriers' frequency matches the applied field's frequency, peak values for the tangent of the loss angle are achieved. Furthermore, at lower frequencies, the grain boundaries play a more significant role, necessitating greater energy for the charge carriers to mobilize. Consequently, energy loss is pronounced at lower frequencies, leading to elevated tanδ values in the low-frequency range.

At higher frequencies, the spreading and directing of granules become more efficient, resulting in lower energy loss due to the minimal energy needed to transfer charge carriers. Consequently, tanδ values are reduced at higher frequencies [21]. It is worth mentioning that the PBLTO compound exhibits the lowest value. In contrast, A1, A2, and MCFO show different behavior compared to the real and imaginary dielectric constants.

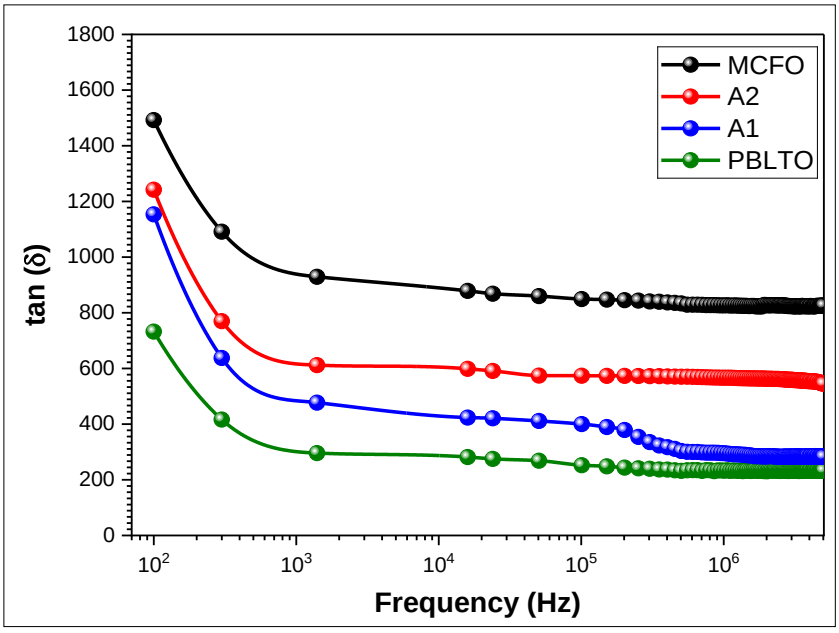

Fig 9: Variation of dielectric loss (tanδ) with frequency for MCFO, PBLTO, A1 and A2 respectively

3.4 Analysis of magnetic properties

Figure 10 displays the hysteresis loops for MCFO, A1, and A2 compounds. These loops illustrate the relationship between the applied magnetic field and the resulting magnetization in the materials. As observed in figure 10, the saturation magnetization (M_s), which represents the maximum magnetization achievable, increases with the increasing ferrite phase content. Additionally, we observe from the graphs that the magnetic field value at which magnetization reaches saturation does not vary significantly in the MCFO models A1 and A2. This increase is attributed to the incorporation of a non-magnetic element, Cd^{+2}. The magnetic hysteresis observed in compounds is a result of magnetic granules (ferrite phase) dispersed in a matrix of non-magnetic granules (BTO phase). The magnetization behavior of Mg-Cd ferrite can be explained by the cation distribution, where (Cd^{+2}) ions occupy tetrahedral sites (site-A) and (Mg^{+2}) ions occupy octahedral sites (B-site) in the AB_2O_4 spin ferrite structure. The saturation magnetization values (M_s) decrease as the ferroelectric phase content (BTO) increases, as evidenced in compounds A1 and A2, correlating with the reduction in ferrite phase content within the compound [22, 23].

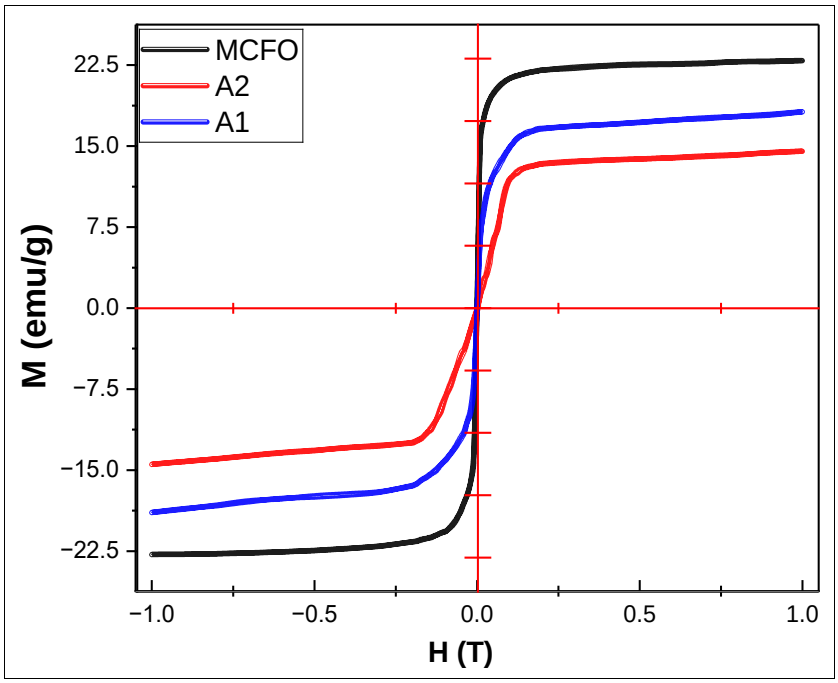

Fig 10: hysteresis loops for MCFO, A1, and A2 compounds, respectively

The isotherm of the magnetization M(H) for the compound MCFO, A2, and A1 shows that our sample presents a ferromagnetic behaviour at room temperature (Figure 11). We notice that when the applied magnetic field increases, the material passes from a weakly magnetized state to a strongly magnetized state, the compound reaches their magnetization saturation M_0 very quickly, which confirms their ferromagnetic behaviour. The Mg–Mg and Mg–O exchange interactions are favoured. This induces the alignment of magnetic spins and promotes ferromagnetism in this compound. M_0 is obtained by extrapolating the value of the magnetization when it no longer varies, as can be seen on the manganite magnetization curve shown. The latter presents the isothermal magnetization curve measured at room temperature from 0 to 1 T for our sample (see figure 11).

The sample shows ferromagnetism at this temperature, nearly saturating at 1 T. Thus, the saturation magnetization for this sample is about 22.8, 17.5 and 14.95 uem/g for the MCFO, A2, and A1 compounds respectively. However, the saturation magnetization of the sample was determined by extrapolation made in the strong field range according to the equation [24].

$$M(H) = M_0\left(1 - \frac{a_2}{(H+H_u+H_{ex})^2}\right) \text{ With } a_2 = \frac{H_r^2}{15} = \frac{1}{15}\left(\frac{2K_L}{M_0}\right)^2$$

Where H is the magnetic field applied to (T), M_0 is the saturation magnetization (emu/g), H_u is the coherent field, H_{ex} is the exchange field, H_r is the random local anisotropy field and a_2 is a constant which is a function of local anisotropy K_L and M_0. Using the fit of magnetization versus applied magnetic field using the equation 2, we obtain M_0 equal to 22.8, 17.5 and 14.955 uem/g for the MCFO, A2, and A1 compounds respectively (Figure 11).

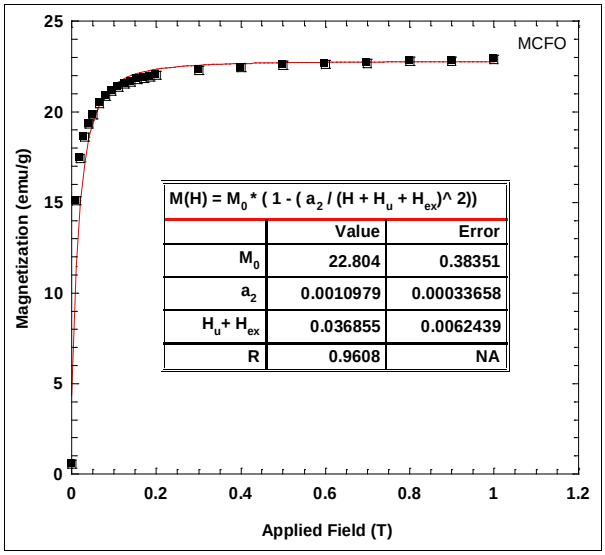

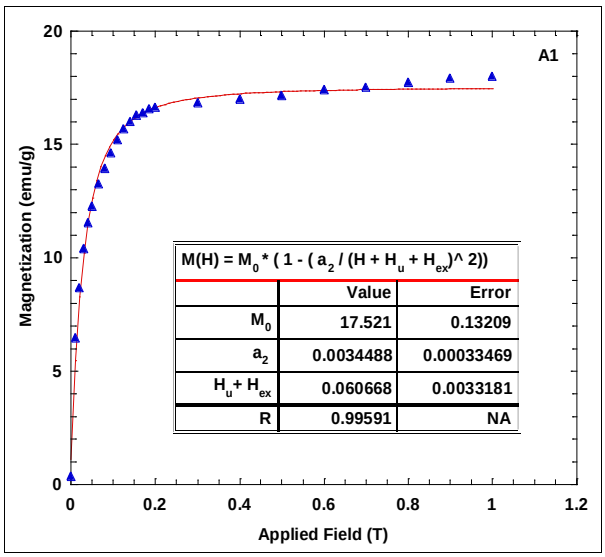

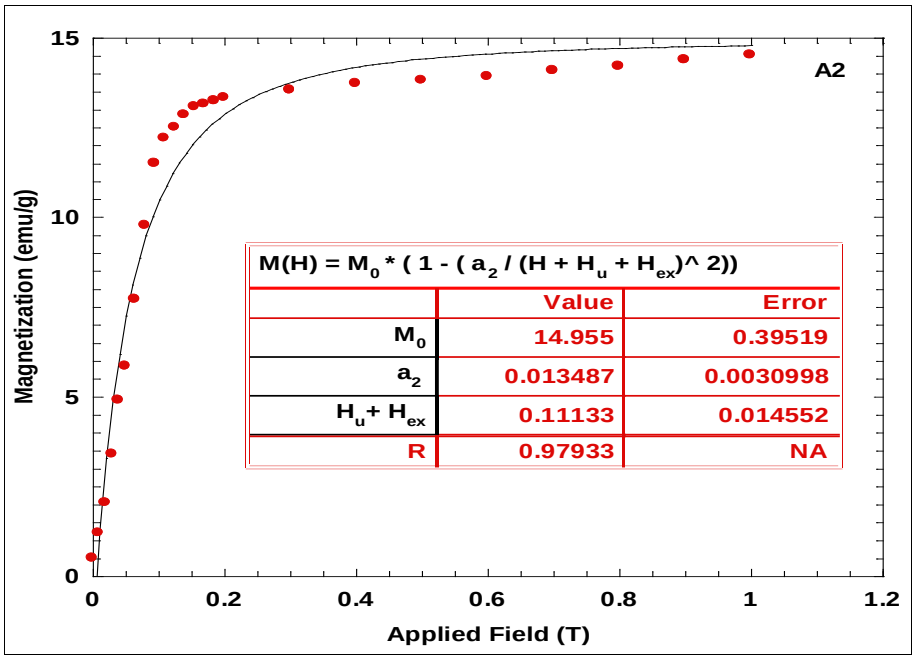

Fig 11: Fit of magnetization (line) as a function of magnetic field applied at room temperature for MCFO, A1and A2 compounds, respectively

4. Conclusion

The study showcases the multifaceted advancements in materials science and engineering, particularly focusing on the synthesis and characterization of composite materials. These composites, formed by combining distinct materials or phases, exhibit exceptional properties surpassing those of individual components. The versatility of these materials, with tailorability to specific application needs, underscores their significance in various fields. Nanoscience and nanotechnology further extend the horizon, exploring unique material properties at the nanoscale. The co-precipitation method emerges as a promising synthesis approach due to its efficiency and minimal sintering requirements, making it ideal for studying material properties. Synthesis experiments on ferrite nanoparticles reveal intriguing findings regarding lattice constants, magnetic properties, and crystallite sizes, shedding light on their structural intricacies. Moreover, thorough analyses via XRD, SEM, and EDAX corroborate structural and morphological characteristics, while dielectric and magnetic property assessments unveil insightful behavior under varying conditions. These comprehensive investigations contribute valuable insights into the intricate world of composite materials, paving the way for further advancements and applications in diverse fields.

5. References

1. Nahas MN. New development in composite materials-recyclable and environment friendly composite materials. Engineering Sciences, 2005, 16(1).
2. Khanna OP. A Text Book of Material Science and Metallurgy. Dhanpat Rai; c2015.
3. Agrawal DC. Introduction to nanoscience and nanomaterials. World Scientific Publishing Company; c2013.
4. Viswanathan B. Physical and Chemical Methods for Synthesis of Nanomaterials. National Centre for Catalysis Research Dept. of Chemistry IIT Madras; c2007.
5. Sathishkumar G, Venkataraju C, Sivakumar K. Synthesis, Structural and Dielectric Studies of Nickel Substituted Cobalt-Zinc Ferrite. Materials Sciences and Applications. 2010;1:19-24.
6. Yadavalli T, Jain H, Chandrasekharan G, Chennakesavulu R. Magnetic hyperthermia heating of cobalt ferrite nanoparticles prepared by low temperature ferrous sulfate-based method. AIP Advances, 2016, 6(5).
7. Hossain MS, Hoque SM, Liba SI, Choudhury S. Effect of synthesis methods and a comparative study of structural and magnetic properties of zinc ferrite. AIP Advances. 2017;7:105321.
8. Zhang S, Li L, Kumar A. Materials characterization techniques. CRC press; c2008.
9. Joshi S, *et al*. Nickel substitution induced effects on gas sensing properties of cobalt ferrite nanoparticles. J. of Alloys and Comp. 2016;654:460-466.
10. Lassoued A, Li JF. Magnetic and photocatalytic properties of Ni–Co ferrites. Solid State Sciences. 2020;104:106199.
11. Pabst W, Gregorova E. Characterization of particles and particle systems. ICT Prague; c2007.
12. Hossain AKM, *et al*. Structural, AC, and DC magnetic properties of Zn1−xCoxFe2O4. Journal of Physics and Chemistry of Solids. 2007;68(10):1933-1939.
13. Rodriguez-Carvajal J. Physica B. 1993;192:55.
14. Rodriguez-Carvajal J, Roisnel T. Line broadening analysis using Full Prof. determination of microstructural properties. In: Materials Science Forum. 2004; 443:123-126.
15. Passerini L. Ricerche sugli spinelli. II. I composti: $CuAl_2O_4$; $MgAl_2O_4$; $MgFe_2O_4$; $ZnAl_2O_4$; $ZnCr_2O_4$; $ZnFe_2O_4$; $MnFe_2O_4$. Gazz Chim. Ital. 1930;60:389-399.
16. Williamson GK, Hall WH. Acta Met. 1953;1:22.
17. Naseri MG, Saion EB, Ahangar HA, Shaari AH. Materials Research Bulletin. 2013;48:1439.
18. Gowreesan S, Kumar AR. Effects of Mg2+ ion substitution on the structural and electric studies of spinel structure of Co1−xMgxFe2O4. Journal of Materials Science: Materials in Electronics. 2017;28:4553-4564.
19. Arjmand M. Electrical conductivity, electromagnetic interference shielding and dielectric properties of multi-walled carbon nanotube/polymer composites. University of Calgary; c2014.
20. Application Note, A. Basics of Measuring the Dielectric Properties of Materials. Printed in USA; c2006. p. 3-15.
21. Gul IH, Maqsood A. Influence of Zn–Zr ions on physical

and magnetic properties of co-precipitated cobalt ferrite nanoparticles. Journal of magnetism and magnetic materials. 2007;316(1):13-18.
22. Farea MM, Kumar S, Batoo KM, Yousef A, Lee CG, Alimuddin, *et al*. J Alloys Comp. 2009;469:451-457.
23. Roy PK. Influence of Substitutions and Sintering Aids on Structural and Electromagnetic Properties of NiCuZn Ferrites. Ph.D., National Institute of Technology; c2009.
24. Loudghiri E, Roky K, Hassini A, Belayachi A, Lassri H. Magnetic properties of amorphous Gd0.67Y0.33. Physica. B: Condensed Matter. 2004;353(1-2):53-58.